CRYSTAL GROWTH & DESIGN

Article

pubs.acs.org/crystal

Broadly Tunable AlInAsSb Digital Alloys Grown on GaSb

Scott J. Maddox,* Stephen D. March, and Seth R. Bank

Microelectronics Research Center and Department of Electrical and Computer Engineering, The University of Texas at Austin, Austin, Texas 78758, United States

ABSTRACT: $Al_xIn_{1-x}As_ySb_{1-y}$ digital alloys lattice-matched to GaSb were grown within the miscibility gap by molecular beam epitaxy, with aluminum fractions ranging from 0% to 80%. Photoluminescence spectra from $Al_xIn_{1-x}As_ySb_{1-y}$ films and from $Al_xIn_{1-x}As_ySb_{1-y}$/GaSb type-II superlattices were used to determine the direct bandgap and the band offsets as a function of the aluminum fraction. Varying the aluminum content tuned the direct bandgap from 0.25 eV (0% aluminum) to 1.24 eV (75% aluminum), corresponding to photon wavelengths from 5000 to 1000 nm, with the transition from direct-gap to indirect-gap occurring at ~1.18 eV (~72% aluminum), or 1050 nm. This direct-gap tuning range of 0.93 eV is the largest reported for a III−V alloy lattice-matched to a commercially available substrate. The broadly tunable bandgap and type-I band alignments of this lattice-matched quaternary make it attractive for advanced mid-infrared and near-infrared detectors and sources.

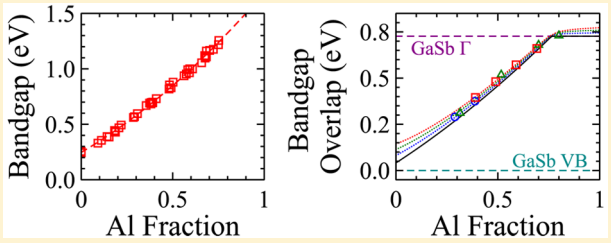

INTRODUCTION

Despite the many possible applications for $Al_xIn_{1-x}As_ySb_{1-y}$ alloys lattice-matched to GaSb (henceforth referred to as AlInAsSb) in mid-infrared (IR) and near-IR optoelectronic devices, the growth and optoelectronic properties of this alloy have remained largely unexplored, due mostly to the presence of a wide miscibility gap.[1−3] Mostly, InAs/AlSb superlattices have been utilized in place of AlInAsSb, such as in interband cascade lasers.[4−7] However, some recent work has demonstrated methods for achieving high quality AlInAsSb films. Zederbauer et al. have improved AlInAsSb random alloy growth on InAs,[8] which exhibits similar challenges to growth on GaSb. Most pertinent to the work described here, though, Vaughn et al. have recently shown that stable AlInAsSb can be grown well within the miscibility gap by molecular beam epitaxy (MBE) as a digital alloy of the component binaries, AlAs, AlSb, InAs, and InSb.[9−11] Using this approach, mid-IR InAsSb/AlInAsSb type-I diode lasers have previously been demonstrated.[10,11] However, these previous studies were limited to Al fractions ranging from 0% to 40%, and photoluminescence (PL) was only observed up to Al fractions of 30%. In this letter, we report on the growth and optoelectronic properties of AlInAsSb digital alloys with Al fractions ranging from 0% to 80%; we identify the functional dependence of the direct bandgap and band offsets on the Al fraction, as well as a probable transition from direct-gap to indirect-gap at an Al fraction of ~72%. The broad tunability of this lattice-matched alloy opens up new band-engineering opportunities for next-generation mid-IR and near-IR light emitting diodes, lasers, and photodetectors for emerging applications in mid-IR countermeasures, free-space telecommunications, light detection and ranging (LIDAR), multispectral imaging, etc.

EXPERIMENTS AND DISCUSSION

Sample Growth. All samples in this study were grown on undoped (001) GaSb substrates by solid-source MBE, using dual-filament effusion cells to source Al, Ga, and In, a tantalum-catalyzed valved arsenic cracker operated at 850°C to source dimeric As_2,[12] and a catalyst-free (pyrolytic boron nitride) valved antimony cracker operated at 900°C to source monomeric Sb.[13] Dimeric As_2 and monomeric Sb were chosen for the associated improvement in material optical quality.[13,14]

We began by adopting the AlInAsSb digital alloy growth conditions reported by Vaughn et al.[9−11] In particular, the substrate temperature was held at 480 °C as determined by blackbody thermometry (k-Space BandiT), the In and Al fluxes were adjusted so that the growth rates of InAsSb and AlAsSb lattice-matched to GaSb were 0.75 ML/s, the As valve was adjusted so that the As_2/In beam-equivalent pressure (BEP) ratio was 5, and the Sb valve was adjusted so that the Sb/In, Sb/Ga, and Sb/Al BEP ratios were approximately 5, 7, and 13, respectively. Note that the As and Sb valve positions were held constant throughout the digital alloys. We did not observe any signs of significant As leakage around the closed shutter during growth, but we did observe significant accumulation of excess As and Sb in the source pockets; nightly pocket outgassing (i.e., leaving the shutters open, the valves closed, and the cracking zones hot) helped to limit accumulation.

For the digital alloy period, we chose a nominal thickness of 10 monolayers (ML) or 3.05 nm, which was sufficiently thin that the electron and hole wave functions would overlap multiple periods and sufficiently thick that shutter transient effects would be adequately small. The Al fraction, x, was thus

Received: October 26, 2015
Revised: May 19, 2016

DOI: 10.1021/acs.cgd.5b01515
Cryst. Growth Des. XXXX, XXX, XXX−XXX

defined as the sum of the AlSb and AlAs thicknesses divided by 10 ML. At low Al fractions (<15%), the alloys were lattice-matched by altering the As fraction, y, through the InSb/InAs thickness ratio, similar to previous reports.[9−11] In contrast to previous reports, lattice matching was also achieved at higher Al fractions (>30%) by inserting an AlAs layer and adjusting the AlAs/AlSb thickness ratio. Finally, a minimum of 0.1 ML of InSb and a five second Sb soak were inserted before and after each InAs layer, respectively, to enforce InSb-like interfacial bonds between the InAs and AlSb layers; such InSb-like interfaces have been shown to result in smoother interfaces and fewer point defects in InAs/AlSb quantum wells and superlattices than the alternative AlAs-like interfaces.[15,16] The Sb soak time of five seconds was chosen as a compromise between higher PL intensity at shorter soak times and improved high-resolution X-ray diffraction (HR-XRD) digital alloy peak intensities and line widths at longer soak times. The resulting shutter sequence was AlSb, AlAs, AlSb, InSb, InAs, Sb, as shown in Figure 1.

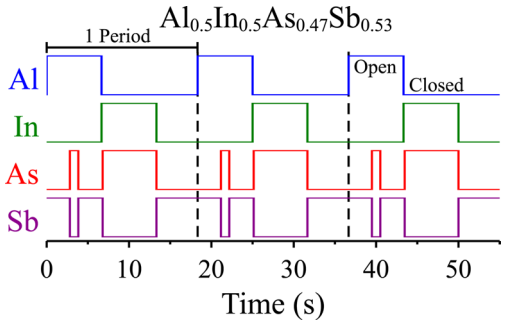

Figure 1. Shutter sequence for three periods of an $Al_{0.5}In_{0.5}As_{0.47}Sb_{0.53}$ digital alloy lattice-matched to GaSb.

The layer structure utilized for both lattice-matching studies and PL studies is shown in Figure 2. The 10 nm thick AlSb

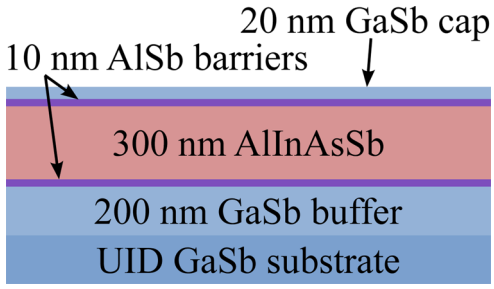

Figure 2. Schematic cross-section of the layer structure investigated.

layers aided PL studies by blocking the diffusion of photo-generated carriers to the top surface and into the GaSb buffer, while the 20 nm GaSb cap protected the underlying AlSb and AlInAsSb from oxidation.

X-ray Diffraction. HR-XRD symmetric $\omega-2\theta$ scans around the GaSb (004) diffraction peak were used to determine the lattice-matching conditions, to measure the actual digital alloy period, and to assess the structural quality. Because of the widely varying lattice constants of the constituent binaries, a shuttering timing error of only 100 ms could alter the strained mismatch by as much as 800 ppm. Consequently, precise, automated control of the shutter timings was critical to achieving repeatable lattice matching. For all of the growths reported in this work, shutter timings were controlled by the AMBER MBE software, which utilizes an external temperature-corrected timing circuit to achieve precise, repeatable shutter timing. In addition, before each growth campaign, the shuttering speeds were calibrated so that each shutter (Al, In, As, and Sb) opened in ∼200 ms and closed in ∼200 ms; this was achieved through an iterative visual calibration method. First, a shutter was cycled between opened and closed several times by computer control, while the calibrator observed the actuation. On the basis of the observations, the calibrator then adjusted the shutter's pneumatic throttle valves to either increase or decrease the actuation speed. If the shutter did not open (close) completely before closing (opening) then the opening (closing) speed was increased. Conversely, if the shutter fully opened (closed) with time to spare, the opening (closing) speed was decreased. This process was repeated until the actuation speed matched the computer controlled cycling speed.

Furthermore, because of the thin layer thicknesses required, a fairly high substrate rotation rate was necessary to minimize layer thickness variations across the substrate. A substrate rotation of 1 revolution every 2 ML, or 22.5 rpm, resulted in sharp digital alloy HR-XRD peaks and strong Pendellösung fringes, as shown in Figure 3, indicating uniform periodicity and

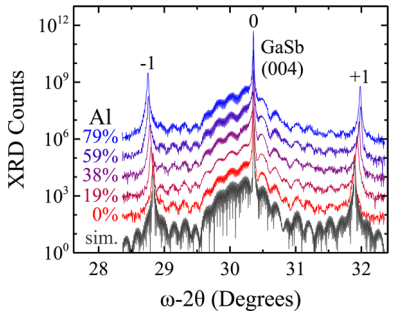

Figure 3. Representative HR-XRD $\omega-2\theta$ scans of five AlInAsSb digital alloys (colored lines, offset vertically) exhibiting sharp digital alloy peaks and excellent agreement with dynamical simulations of a 0% Al structure (black line).

smooth interfaces over the sampled area (∼2 cm wide line beam). The digital alloy periods determined from the digital alloy peak spacing varied from 2.9 to 3.4 nm over the sample set; we attribute the difference between the actual period and the nominal period of 3.05 nm to slight growth-rate miscalibration, shutter transients,[17] and effusion cell flux drift. Linear fitting of the digital alloy period as a function of the nominal Al fraction for several samples grown on the same day provided an estimate of the actual In and Al fluxes. Using these corrected fluxes, we then corrected the nominal Al fractions to first order; all reported Al fractions have been corrected in this manner. Using the procedures described above, and after correcting for flux drift, we have observed repeatable structural and optical properties of each AlInAsSb digital alloy; thus, we are confident that improving effusion cell flux stability will enable extremely accurate and repeatable control of the material properties.

AlInAsSb Photoluminescence. PL spectra were measured using a frequency-doubled Nd:YAG pump laser (532 nm), a nitrogen-purged 0.5 m grating spectrometer, a liquid-nitrogen-cooled InSb detector, and a lock-in amplifier. Swappable diffraction gratings and optical filters were used to select for

DOI: 10.1021/acs.cgd.5b01515
Cryst. Growth Des. XXXX, XXX, XXX−XXX

specific spectral ranges and to attenuate spectrometer inputs from outside of the desired spectral range. All PL spectra are presented in units proportional to the photon flux and have been properly normalized so as to remove the effects of grating efficiency, lens and filter absorption, and spectral variation in the detector quantum efficiency. In addition, when possible, measurements were repeated and confirmed to be accurate with a separate thermoelectrically cooled InGaAs detector.

We observed room temperature PL above the background noise floor from AlInAsSb digital alloys for all Al fractions between 0% and 75%, with bandgaps ranging from approximately 0.25 to 1.24 eV. Several representative PL spectra are shown in Figure 4. Note that the peak at 1.17 eV labeled "second order of pump laser" could alternatively be due to unconverted fundamental Nd:YAG (1064 nm) light.

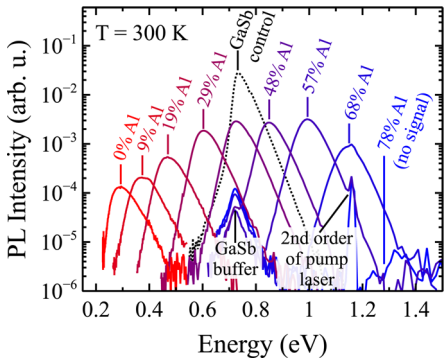

Figure 4. Representative room temperature PL spectra from several AlInAsSb digital alloys. PL above the background noise floor was observed for Al fractions from 0% to 75%.

The bandgaps of the alloys were estimated from the PL peak energies by subtracting an estimate of the thermal carrier-spreading energy, which can vary from kT/2 to 3kT depending on the magnitude of alloy broadening and other effects.[18] In this study, we used the half-widths at half-maximum (HWHM) on the low-energy side of the PL peaks, which varied from 31 to 60 meV (1.2−2.3 kT), as an estimate of the thermal carrier-spreading energy. The resulting experimental bandgap energies are shown in Figure 5, along with the quadratic best fit given by

$$E_g(x) = 0.247 + 0.97x + 0.47x^2 \text{ eV} \quad (1)$$

where x is the Al fraction. Also shown in Figure 5 (in gray), is the bandgap predicted from the recommended band parameters using the standard alloy mixing formula.[19−21] The large disparity between the experimental bandgap and the predicted bandgap is attributable to ordering effects, which the standard alloy mixing formula does not take into account, but which are intrinsic to digital alloys. Similar effects have been predicted and observed in a variety of ordered III−V alloys including GaInP,[22,23] GaInAs,[24] GaAsSb,[25] InAsSb,[26] and GaInAsSb,[27] although the effect is typically small (<100 meV). The large ordering effect present in these AlInAsSb digital alloys implies that the bandgap will depend significantly on the digital alloy period and suggests the potential for additional tuning of the optoelectronic properties.

Applying the Kronig-Penney[28] model to alternating layers of $InAs_{0.91}Sb_{0.09}$ and $AlAs_{0.08}Sb_{0.92}$ can provide a first order correction for these ordering effects, resulting in the predicted bandgap shown by the blue line in Figure 5. Although the Kronig-Penney model provides a more accurate bandgap

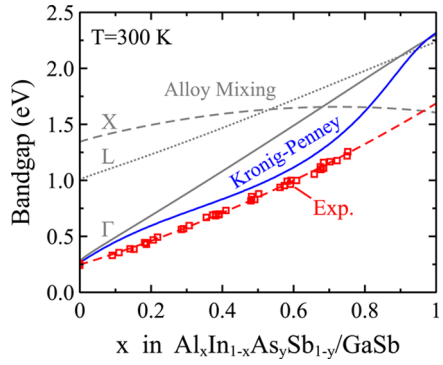

Figure 5. Experimental bandgaps of AlInAsSb digital alloys (red squares), determined from room temperature PL spectra, and the quadratic best fit (red dashed line) given by eq 1. Also shown, for comparison, are the bandgaps predicted from the recommended band parameters[20,21] using the standard alloy mixing formula[19] (gray lines) and by applying the Kronig-Penney[11] model to $InAs_{0.91}Sb_{0.09}$/$AlAs_{0.08}Sb_{0.92}$ (blue line).

prediction than the standard alloy mixing formula, it does not take into account the complex band structure in the bandgap, band-nonparabolicity, interactions with neighboring valence and conduction bands, biaxial strain, or charge carrier decoherence/localization;[27] more accurate corrections should be possible with 8 or 12 band k.p transfer matrix calculations, which can account for all of these effects except charge carrier decoherence/localization.

As the Al fraction was increased above ∼60%, the integrated PL intensity decayed exponentially, as shown in Figure 6. This

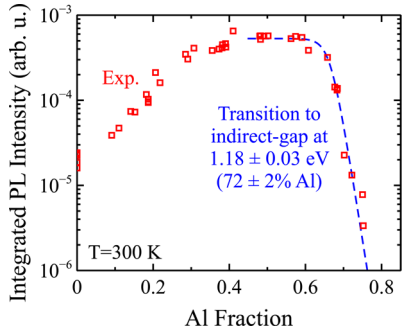

Figure 6. Integrated PL intensity (red squares) from the AlInAsSb digital alloys exhibited a sharp decline at Al fractions above ∼60%, consistent with a transition from direct-gap to indirect-gap. Fitting eq 2 (blue dashed line) yielded an indirect bandgap of ∼1.18 eV, corresponding to a transition at ∼72% Al.

decay could either be due to the spontaneous formation of nonradiative recombination centers at sufficiently high Al fractions or to a transition from direct-gap to indirect-gap. Note that the PL measurements at high Al fractions were repeated with an InGaAs detector to confirm that the decay was not due to detector efficiency. The integrated PL intensity near a direct-indirect transition has a functional dependence on the alloy fraction, x, given by

$$I(x) = \frac{I_0}{1 + g_i \frac{\tau_d}{\tau_i} \frac{m_i^*}{m_d^*} \exp\{[E_g^d(x) - E_g^i(x)]/kT\}} \quad (2)$$

where I_0 is a constant, kT is the thermal energy, g_i is the number of equivalent indirect valleys, τ_d and τ_i are the electron lifetimes,

DOI: 10.1021/acs.cgd.5b01515
Cryst. Growth Des. XXXX, XXX, XXX−XXX

m_d^* and m_i^* are the density-of-states effective masses, and E_g^d and E_g^i are the bandgaps for the direct and indirect valleys, respectively.[29,30] Inserting the experimental $E_g^d(x)$ given by eq 1 and assuming negligible variation in $E_g^i(x)$ resulted in exceptional agreement with the experimental rate of decay of the integrated PL intensity, strongly supporting the conclusion that the decay is due to a transition to indirect-gap.

Using reasonable assumptions, $g_i = g_X = 3$, $m_d^* = m_\Gamma^* = 0.07m_e$, and $m_i^* = m_X^* = 0.4m_e$, we estimated $\tau_d/\tau_i = 1 \pm 1$ and $E_g^i = 1.18 \pm 0.03$ eV through fitting; this indirect-gap energy corresponds to a transition at 72 ± 2% Al. Absorption spectroscopy measurements are needed to confirm these results; however, due to the small bandgap of the GaSb substrate, this will require substrate removal or metamorphic growth on a wider-bandgap substrate, such as GaAs, which is beyond the scope of this letter.

AlInAsSb/GaSb Superlattice Photoluminescence. By utilizing the type-II band alignments between AlInAsSb and GaSb, we were also able to estimate the bandgap overlap and band offsets between these materials, similar to the method described by Hu et al.[31] First, AlInAsSb/GaSb type-II superlattices (SL) with periods of 24 nm, 30 nm, and 43 nm were grown using a layer structure identical to that shown in Figure 2, except with portions of the AlInAsSb layer replaced by GaSb. Note that long SL periodicities were intentionally selected in order to minimize band-filling and quantum-confinement effects. The bandgap overlap, including quantum confinement, was then estimated from the PL peak energies by subtracting the low-energy HWHM, as described above. Example spectra taken at a pump intensity of 2.4 kW/cm^2 are shown in Figure 7. Spectra taken at a lower pump intensity of 240 W/cm^2 exhibited negligibly small redshifts of less than 4 meV.

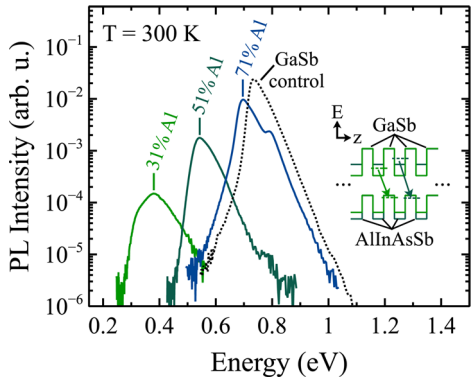

Figure 7. Room temperature PL spectra from three AlInAsSb/GaSb type-II superlattice structures with 30 nm periods. Band diagrams depicting the spatially indirect optical transitions are shown in the inset. The PL peak energy is related to the overlap between the AlInAsSb and GaSb bandgaps, as discussed in the text.

A least-squares best fit to the data, shown in Figure 8, was then determined using a model that included estimates of the finite-well quantum confinement energy for each type-II SL periodicity and Al fraction. Although this simple model does not include band nonparabolicity or interactions between neighboring wells, these higher-order effects are negligible compared to the experimental variation, as evidenced by Figure 8. The best-fit bandgap overlap excluding quantum confinement, shown as the solid black line in Figure 8, is given by

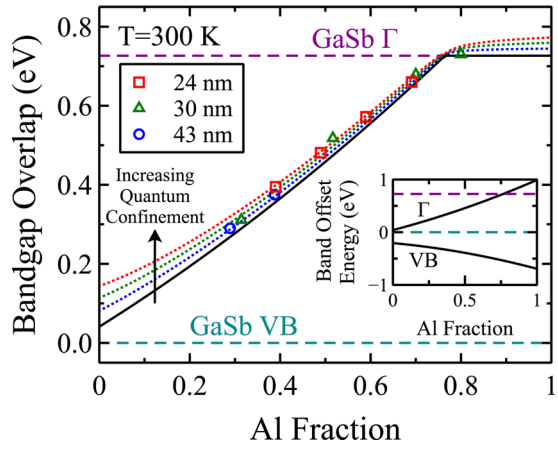

Figure 8. Overlap of the AlInAsSb and GaSb bandgaps estimated using PL from AlInAsSb/GaSb type-II superlattice structures with 24 nm (red squares), 30 nm (green triangles), and 43 nm periods (blue circles). The best fit, given by eq 3, is shown without (solid black line) and with (dotted red, green, and blue lines) quantum confinement added. The extracted band offset energies are shown as a function of Al fraction in the inset. The GaSb Γ−valley minimum (dashed magenta line) and valence band (VB) maximum (dashed cyan line) are shown in both plots, for comparison.

$$E_o(x) = 0.041 + 0.717x + 0.235x^2 \text{ eV} \quad (3)$$

Note that equal band bowing in the conduction and valence bands of the AlInAsSb was assumed for this fit; if this is not a valid assumption then the bandgap overlap at low Al fractions may be higher or lower by as much as 60 meV.

The inset in Figure 8 shows the extracted Γ−valley conduction band and valence band (VB) offset energies for the AlInAsSb digital alloys as a function of the Al fraction. As can be seen, these alloys exhibit type-I band alignments with respect to each other, making them particularly attractive for electrically injected mid-IR type-I diode lasers.

CONCLUSION

In conclusion, we have grown $Al_xIn_{1-x}As_ySb_{1-y}$ digital alloys lattice-matched to GaSb by molecular beam epitaxy and characterized their optoelectronic properties. Varying the Al fraction from 0% to 75% yielded direct-gaps spanning from the mid-IR (0.25 eV, 5000 nm) to the near-IR (1.24 eV, 1000 nm), with a transition from direct-gap to indirect-gap at an Al fraction of ∼72% (1.18 eV, 1050 nm). This direct-gap tuning range of 0.93 eV is the largest reported for a III−V alloy lattice-matched to a commercially available substrate. Such a broadly tunable direct bandgap combined with the type-I band alignments exhibited by this lattice-matched quaternary alloy provides ample opportunities for advanced device engineering of mid-IR and near-IR detectors and sources.

AUTHOR INFORMATION

Corresponding Author

*E-mail: smaddox@utexas.edu.

Notes

The authors declare no competing financial interest.

ACKNOWLEDGMENTS

This work was supported by the Army Research Office (W911NF-12-1-0428).

DOI: 10.1021/acs.cgd.5b01515
Cryst. Growth Des. XXXX, XXX, XXX−XXX

REFERENCES

(1) Onabe, K. *NEC Res. Dev.* **1984**, *72*, 1.
(2) Turner, G. W.; Manfra, M. J.; Choi, H. K.; Connors, M. K. *J. Cryst. Growth* **1997**, *175*−*176* (Part 2), 825.
(3) Semenov, A. N.; Solov'ev, V. A.; Meltser, B. Y.; Terent'ev, Y. V.; Prokopova, L. G.; Ivanov, S. V. *J. Cryst. Growth* **2005**, *278*, 203.
(4) Meyer, J. R.; Vurgaftman, I.; Yang, R. Q.; Ram-Mohan, L. R. *Electron. Lett.* **1996**, *32*, 45.
(5) Kim, C. S.; Kim, M.; Abell, J.; Bewley, W. W.; Merritt, C. D.; Canedy, C. L.; Vurgaftman, I.; Meyer, J. R. *Appl. Phys. Lett.* **2012**, *101*, 061104.
(6) Shterengas, L.; Hosoda, T.; Wang, M.; Feng, T.; Kipshidze, G.; Belenky, G. *Proc. SPIE* 2016, *9767*, 976703-976703−8.
(7) Hosoda, T.; Feng, T.; Shterengas, L.; Kipshidze, G.; Belenky, G. *Appl. Phys. Lett.* **2016**, *108*, 131109.
(8) Zederbauer, T.; Andrews, A. M.; MacFarland, D.; Detz, H.; Schrenk, W.; Strasser, G. *Photonics* **2016**, *3*, 20.
(9) Vaughn, L. G.; Dawson, L.; Ralph; Xu, H.; Jiang, Y.; Lester, L. F. *Mater. Res. Soc. Symp. Proc.* **2003**, M7.2.1−M7.2.12.
(10) Vaughn, L. G.; Dawson, L. R.; Pease, E. A.; Lester, L. F.; Xu, H.; Jiang, Y.; Gray, A. L.*Phys. Simul. Optoelectron. Devices XIII 307*, 2005.
(11) Vaughn, L. G.*Mid-Infrared Multiple Quantum Well Lasers Using Digitally-Grown Aluminum Indium Arsenic Antimonide Barriers and Strained Indium Arsenic Antimonide Wells*, Ph.D. Dissertation, The University of New Mexico, 2006.
(12) Garcia, J. C.; Barski, A.; Contour, J. P.; Massies, J. *Appl. Phys. Lett.* **1987**, *51*, 593.
(13) Brewer, P. D.; Chow, D. H.; Miles, R. H. *J. Vac. Sci. Technol., B: Microelectron. Process. Phenom.* **1996**, *14*, 2335.
(14) Miles, R. H.; Chow, D. H.; Zhang, Y.-H.; Brewer, P. D.; Wilson, R. G. *Appl. Phys. Lett.* **1995**, *66*, 1921.
(15) Tuttle, G.; Kroemer, H.; English, J. H. *J. Appl. Phys.* **1990**, *67*, 3032.
(16) Bennett, B. R.; Shanabrook, B. V.; Glaser, E. R. *Appl. Phys. Lett.* **1994**, *65*, 598.
(17) Gozu, S.; Mozume, T.; Kuwatsuka, H.; Ishikawa, H. *Nanoscale Res. Lett.* **2012**, *7*, 620.
(18) Hunter, A. T.; McGill, T. C. *J. Appl. Phys.* **1981**, *52*, 5779.
(19) Glisson, T. H.; Hauser, J. R.; Littlejohn, M. A.; Williams, C. K. *J. Electron. Mater.* **1978**, *7*, 1.
(20) Vurgaftman, I.; Meyer, J. R.; Ram-Mohan, L. R. *J. Appl. Phys.* **2001**, *89*, 5815.
(21) Adachi, S. *J. Appl. Phys.* **1987**, *61*, 4869.
(22) Gomyo, A.; Suzuki, T.; Iijima, S. *Phys. Rev. Lett.* **1988**, *60*, 2645.
(23) Kurtz, S. R.; Olson, J. M.; Kibbler, A. *Appl. Phys. Lett.* **1990**, *57*, 1922.
(24) Arent, D. J.; Bode, M.; Bertness, K. A.; Kurtz, S. R.; Olson, J. M. *Appl. Phys. Lett.* **1993**, *62*, 1806.
(25) Kawamura, Y.; Gomyo, A.; Suzuki, T.; Higashino, T.; Inoue, N. *Jpn. J. Appl. Phys.* **2002**, *41*, L447.
(26) Wei, S.-H.; Zunger, A. *Appl. Phys. Lett.* **1990**, *56*, 662.
(27) Kaspi, R.; Donati, G. P. *J. Cryst. Growth* **2003**, *251*, 515.
(28) de L. Kronig, R. L.; Penney, W. G. *Proc. R. Soc. London, Ser. A* **1931**, *130*, 499.
(29) Onton, A.; Chicotka, R. J. *J. Appl. Phys.* **1970**, *41*, 4205.
(30) Shah, J.; Miller, B. I.; DiGiovanni, A. E. *J. Appl. Phys.* **1972**, *43*, 3436.
(31) Hu, J.; Xu, X. G.; Stotz, J. a. H.; Watkins, S. P.; Curzon, A. E.; Thewalt, M. L. W.; Matine, N.; Bolognesi, C. R. *Appl. Phys. Lett.* **1998**, *73*, 2799.

DOI: 10.1021/acs.cgd.5b01515
Cryst. Growth Des. XXXX, XXX, XXX−XXX